Journal of Alloys and Compounds 817 (2020) 152777

Contents lists available at ScienceDirect

Journal of Alloys and Compounds

journal homepage: http://www.elsevier.com/locate/jalcom

Elevated temperature microstructure evolution of a medium-entropy CrCoNi superalloy containing Al,Ti

C.E. Slone [a, b, *], E.P. George [c, d], M.J. Mills [a, b]

[a] Center for Electron Microscopy and Analysis, The Ohio State University, Columbus, OH, 43212, USA
[b] Department of Materials Science and Engineering, The Ohio State University, Columbus, OH, 43210, USA
[c] Materials Science and Technology Division, Oak Ridge National Laboratory, Oak Ridge, TN, 37831, USA
[d] Materials Science and Engineering Department, University of Tennessee, Knoxville, TN, 37996, USA

ARTICLE INFO

Article history:
Received 30 July 2019
Received in revised form
12 October 2019
Accepted 22 October 2019
Available online 24 October 2019

Keywords:
Medium-entropy alloy
CrCoNi
Ni-base superalloy
Microstructural stability
Phase decomposition

ABSTRACT

A new medium-entropy superalloy was produced based on the compositions of equiatomic CrCoNi and Ni-base superalloy Inconel 740H. Initial alloy design was performed using Thermo-Calc. The aging response and microstructural stability were assessed following heat treatment at temperatures between 600 and 900 °C and durations up to 100 h. Aging from a fully recrystallized state resulted in negligible grain growth and produced γ' and σ phases. The same phases were present after aging from a cold-rolled state, but partially recrystallized microstructures resulted in multi-modal size distributions and heterogeneous spatial arrangements. Room temperature hardness measurements were used to correlate aging conditions with quantitative precipitate measurements and mechanical properties.

1. Introduction

Medium- and high-entropy alloys (MEAs/HEAs) have recently demonstrated excellent low-temperature mechanical properties, making them attractive candidates for structural applications at cryogenic and room temperatures [1–6]. The driving concept behind these diverse compositions is the use of multiple principal elements, which nominally increase the configurational entropy of structurally simple solid solution phases and stabilize them at the expense of complex, brittle intermetallic phases. Although the concept of entropic stabilization has been convincingly challenged [6–8], many new alloy compositions have been explored and several other potential benefits of highly alloyed, multi-principal element (MPE) alloys remain compelling.

One early hypothesis for high-entropy alloys was the existence of a "sluggish diffusion" effect, which posits that vacancy formation and migration kinetics in multi-principal element alloys are slowed due to local variations in lattice potential energy (induced by the presence of different types of atoms on every lattice site) [9,10]. This has important consequences for alloy behavior at elevated temperatures, since deleterious effects like particle coarsening [11] and creep deformation [12] are usually rate-limited by diffusion. Most work at elevated temperatures has focused on refractory high-entropy alloys with body-centered cubic (bcc) structures [13–16], although there have recently been several studies involving face-centered cubic (fcc) alloys [17,18], including measurements of diffusion rates [10] and creep deformation [19] in the ubiquitous CrFeMnCoNi system. Although CrFeMnCoNi demonstrated lower creep rates and higher activation energies than some common high-temperature ferritic/martensitic steels, it also exhibits phase decomposition after prolonged exposure to elevated temperatures [20,21], even in the absence of prior deformation [22]. It is therefore unclear whether these alloys might be suitable for applications at such temperatures.

Load-bearing applications at temperatures from approximately 650 °C–900 °C typically utilize polycrystalline Ni-base superalloys [23–26]. At lower temperatures in that range, solid solution alloys can be used (although these may benefit from low volume fractions of grain boundary carbides, e.g, Refs. [27,28]), while temperatures above approximately 700 °C require substantial additional strengthening via precipitation of the ordered $Ni_3(Al,Ti)$ γ' phase [29–31]. Modern Ni-base superalloys often contain large quantities

* Corresponding author. Center for Electron Microscopy and Analysis, The Ohio State University, Columbus, OH, 43212, USA.
E-mail address: slone.103@osu.edu (C.E. Slone).

https://doi.org/10.1016/j.jallcom.2019.152777
0925-8388/

of Cr and Co for corrosion resistance and solid solution strengthening of the matrix phase, respectively [26]. Alloys comprising high concentrations of the elements Ni, Cr, and Co are also abundant in the MEA and HEA literature; for example, equiatomic CrMnFeCoNi [32–35] and CrCoNi [36–40] alloys have been extensively studied.

Given the compositional similarities described above, it is interesting and useful to assess the microstructure and high-temperature stability of an alloy resulting from the union of MPE and Ni-base superalloy concepts. One major question is whether these fcc alloys can sustain stable microstructures (i.e. resist formation of deleterious phases) at elevated temperatures despite substantial alloying additions. This has previously presented a significant obstacle in the development of more conventional superalloys like Inconel 740 (a precursor to the current alloy Inconel 740H), even though it contains less Cr and Co and is therefore less highly alloyed than a typical MPE composition [41,42]. A second critical question is whether commonly employed thermodynamic calculation software packages like Thermo-Calc can generate useful predictions for these systems, which will be critical for expediting future development and refinement of new highly alloyed compositions.

In the present work, a new medium-entropy, multi-principal element alloy was designed using Thermo-Calc and aged under different conditions to assess the evolution of important parameters such as grain size and γ' precipitate size and volume fraction. Identical aging treatments were also performed on heavily cold-rolled material to evaluate the propensity for recrystallization or phase decomposition in the presence of deformation. The results were compared to equilibrium calculations and non-equilibrium, isothermal aging simulations in Thermo-Calc.

2. Materials and methods

2.1. Thermo-Calc simulations

Thermodynamic simulations for alloy design were performed using Thermo-Calc Software (version 2018b.27179) with all default phases in the Ni-based superalloys package (TCNI8, MOBNI4). After a target alloy composition (Table 1) was chosen for fabrication and testing, as described in the Results section, simulations were performed again with the analyzed composition of the final alloy given in Table 1.

For TC-PRISMA simulations, which incorporate kinetic considerations, isothermal calculations were performed to simulate up to 100 h of aging at 700 °C, 800 °C, and 900 °C. The disordered γ matrix phase was defined as FCC_L12 and possible precipitate phases were defined as FCC_L12#2 (bulk nucleation), FCC_L12#3 (bulk nucleation), M23C6 (grain boundary nucleation), and σ-phase (grain boundary nucleation). FCC_L12#2 and FCC_L12#3 can be either the ordered γ' phase or disordered MC-type carbides and were distinguished based on site occupancy (where equal site occupancy indicates a disordered phase) and chemical composition. Interfacial energies for all precipitate phases were calculated by TC-PRISMA and molar volumes were automatically extracted from the Thermo-Calc database. The Thermo-Calc simplified growth rate model was used assuming a spherical morphology.

Table 1
Composition of alloy V1.

	Ni	Cr	Co	Al	Ti	Nb	C
Target Composition (at%)	31.0	30.6	31.1	4.1	2.3	0.9	-
Analyzed Composition (at%)	30.8	30.6	31.3	4.1	2.3	0.9	0.05
Analyzed Composition (wt%)	32.6	28.7	33.3	2.0	2.0	1.5	0.0001

Note: totals are not always 100% because of rounding errors.

2.2. Material

Processing steps for the alloy are summarized in Fig. 1. The alloy was produced by arc melting constituent elements in a water-cooled copper hearth under Ar atmosphere. The purities of the added elements were 99.99% (Cr and Al), 99.9% (Ni), and 99.6% (Nb). The added Ti was commercial purity grade with O less than 590 ppm and C less than 110 ppm. As shown in Table 1, 0.05 at% C was picked up as an impurity during the melting process, most likely from the other raw materials.

During arc melting, ingots were flipped and re-melted five times before being drop-cast into a copper mold. The as-cast ingots were homogenized and solutionized for 24 h at 1473 K (1200 °C) and water-quenched to avoid precipitation of gamma prime or other phases during cooling. Ingots were then cold-rolled ~70% to a final thickness of 6 mm. Following rolling, plates with approximate dimensions 7.5 mm long x 6 mm wide x 6 mm thick were cut from the ingots by electrical discharge machining with the long direction parallel to the rolling axis. Some specimens were then subjected to an additional recrystallizing/solutionizing heat treatment of 10 min at 1323 K (1050 °C) followed by a water quench, which produced fully recrystallized microstructures. Both sets of samples (as-rolled and fully recrystallized) therefore started as solutionized material nominally free of gamma prime precipitates. Both conditions were subsequently given identical aging treatments at temperatures between 600 and 900 °C for 1–100 h.

2.3. Microstructure characterization

Pre- and post-deformation specimens were prepared for study in the SEM using a parallel polisher and 400-, 600-, 800-, and 1200-grit SiC papers. A final chemo-mechanical polish was performed using 50 nm colloidal silica.

Specimens were examined using a Thermofisher/FEI Apreo scanning electron microscope (SEM). Electron backscatter diffraction (EBSD) orientation mapping was performed using an EDAX Hikari Super EBSD camera in conjunction with acquisition software EDAX TSL DC7 and analysis software EDAX TSL OIM 8 [43]. Scans were acquired using an accelerating voltage of 20 kV and a beam current of 6.4 nA at a working distance of 20 mm. Local alloy chemistry was measured using semi-quantitative X-ray energy dispersive spectroscopy (EDS).

X-ray diffraction was performed using a Rigaku SmartLab with a Ge (220)×4 4-bounce diffracted beam monochromator and Cu Kα radiation ($\lambda = 0.154$ nm). Scans were performed over a 2θ angular range of 20–100° with a step size of 0.01° and scan speed 0.1° min^{-1}.

2.4. Mechanical characterization

Following heat treatment, specimens for hardness testing were mechanically polished using 400-, 600-, 800-, and 1200-grit SiC paper. Hardness measurements were made on a Leco LM-100AT microhardness tester with a loading force of 100 g and dwell time of 25 s. For each specimen, two arrays of 6 × 6 indents were made at separate locations on the specimen for a total of 72 measurements per condition. The spacing between indents was 100 μm and the typical size of each indent on the surface was on the order of 20 μm.

3. Results

3.1. Alloy design and Thermo-Calc simulations

The primary objective in designing the alloy for this work was to combine the potential benefits of equiatomic alloys from the HEA/

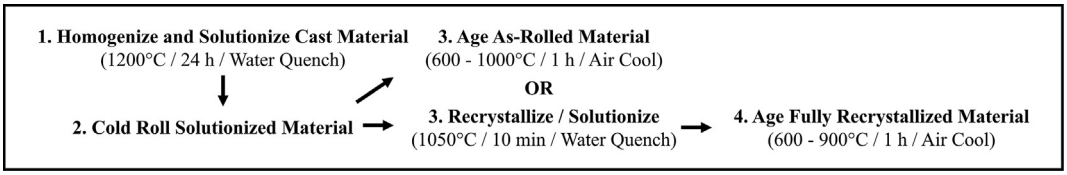

Fig. 1. Processing steps used in this work. The aging response was examined in the as-rolled and fully recrystallized conditions.

MPE literature with the high-temperature capabilities of conventional superalloys. Equiatomic CrCoNi was chosen as one basis due to its inherent similarity to many superalloy compositions, in addition to its outstanding capacity for work hardening and excellent room-temperature tensile strength. Superalloy Inconel 740H was selected as a second basis due to its high Cr and Co content, and previous reports showing similar room-temperature behavior between that alloy [44] and equiatomic CrCoNi [40]. The basic principle therefore involved increasing the Cr and Co content in alloy 740H to approach equiatomic proportions.

One important consideration was that the new alloy, henceforth referred to as V1, should be capable of forming a single-phase solid solution after an appropriate heat treatment above the γ′ solvus temperature, and maintain that state after rapid quenching. This produces a much softer, precipitate-free microstructure that can be rolled in a condition closely matching equiatomic CrCoNi to produce similar deformation structures. Fig. 2a shows Thermo-Calc simulations for the equilibrium composition of the disordered γ matrix phase across a range of temperatures. Above approximately 1008 °C (the predicted γ' solvus temperature), the equilibrium matrix is predicted to contain equal proportions of Ni, Cr, and Co with additional Al, Ti, and Nb in solution. In the presence of carbon, some of the Ti and Nb also form MC-type carbides. If properly quenched, this solid-solution microstructure (with incidental carbides) will be preserved at room temperature.

Fig. 2b shows predictions for the equilibrium mole fractions of different phases across a range of temperatures. Of particular note are the ordered γ' phase (dark blue) and σ phase (gray) beginning at 1008 °C and 970 °C, respectively. The predicted amount of σ phase is very large as a result of the high Cr content, and actually exceeds that of the γ matrix phase below 570 °C. Equilibrium phases that are predicted to develop at lower temperatures are unlikely to be observed due to kinetic limitations; however, it is interesting to note that a hexagonal close-packed (hcp) structure (purple) is predicted as the dominant stable phase at cryogenic temperatures. Equiatomic CrCoNi readily undergoes nanoscale fcc to hcp transformations during cryogenic deformation [38] and it has been suggested that the hcp phase is actually more thermodynamically stable in that temperature regime [39].

Fig. 3 shows simulated isothermal aging curves up to 100 h at 800 °C and 900 °C. These simulations, performed with the precipitation module (TC-PRISMA) in Thermo-Calc, are non-equilibrium calculations incorporating kinetic considerations. Fig. 3a shows evolution of the volume fractions of γ′, σ, and MC carbide phases. The carbide fraction remains small at both temperatures due to low carbon levels in the alloy. For both γ′ and σ phase, predicted volume fractions were higher at 800 °C (~0.24 and 0.22, respectively) than at 900 °C (~0.16 and < 0.01, respectively). Fig. 3b shows predicted coarsening behavior for the γ' phase, which is plotted as the cube of the precipitate radius against time in accordance with the well-known LSW theory of Ostwald ripening by Lifshitz and Slyozov [45] and Wagner [46]. As expected, higher coarsening rates were predicted at 900 °C than 800 °C with precipitate diameters of 65 nm and 27 nm, respectively, after aging for 1 h. Precipitates were predicted to coarsen to diameters of 313 nm and 126 nm after aging for 100 h.

3.2. Microstructure of solutionized/fully recrystallized material

The microstructure after rolling, recrystallizing/solutionizing, and quenching, is shown in Fig. 4. As measured via linear intercept method, the average grain size in the solutionized and quenched material was 59 ± 3 μm (standard error). Fig. 4a shows an inverse pole figure map of the alloy with color corresponding to the surface

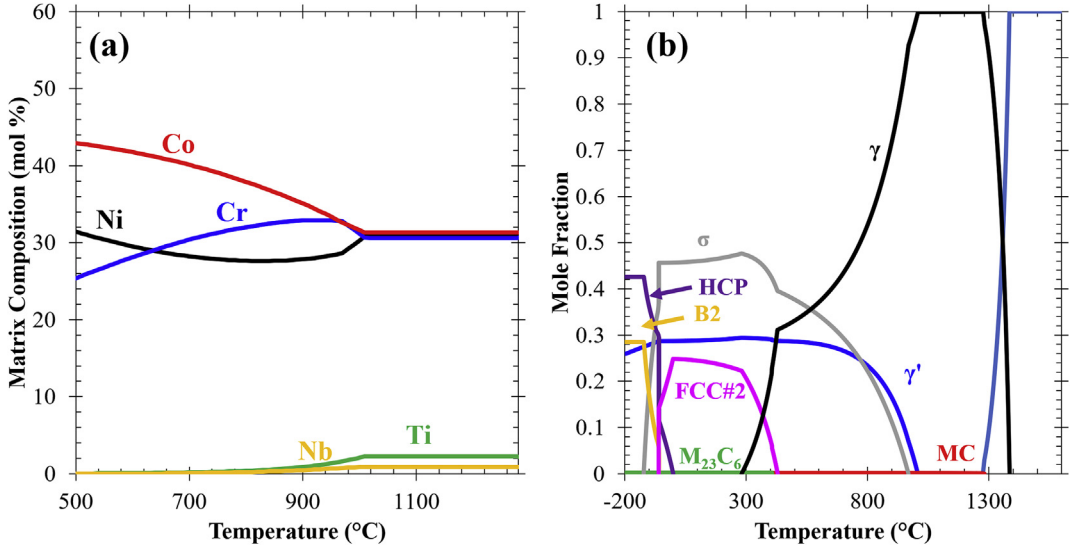

Fig. 2. Equilibrium Thermo-Calc simulations showing, as a function of temperature, (a) the composition of the γ matrix phase, and (b) mole fractions of the equilibrium phases.

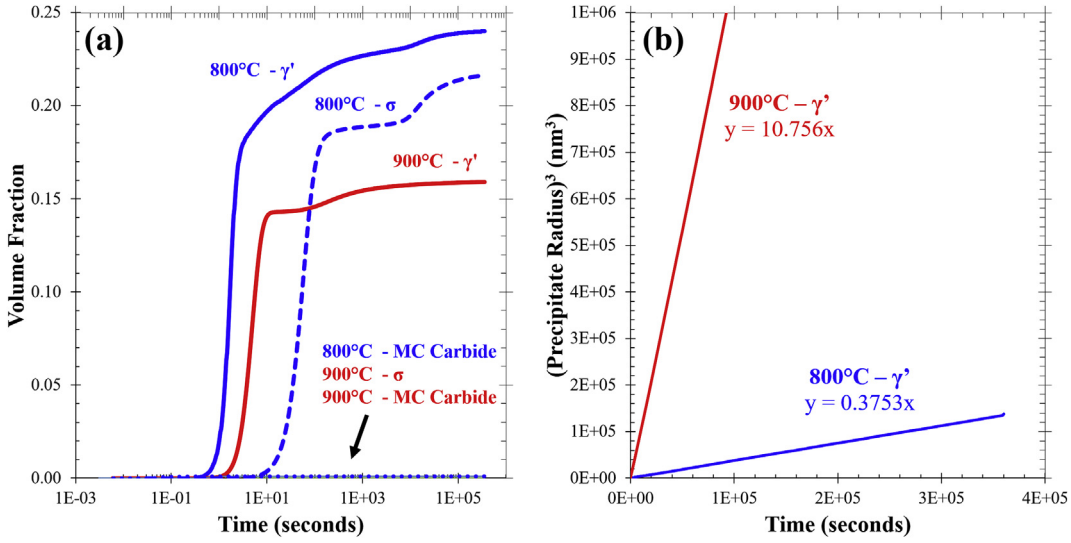

Fig. 3. Simulated evolution of phases during isothermal aging at 800 °C (blue) and 900 °C (red) up to 100 h. (For interpretation of the references to color in this figure legend, the reader is referred to the Web version of this article.)

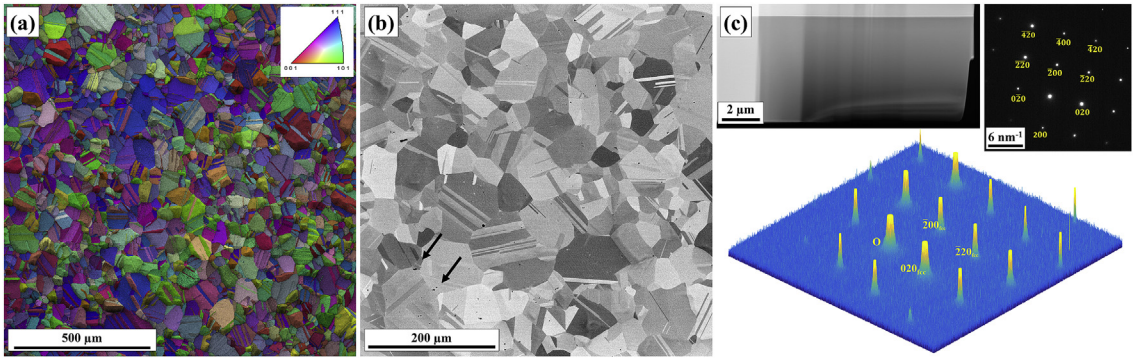

Fig. 4. Fully recrystallized microstructure following solutionizing and quenching. (a) Inverse pole figure map showing equiaxed grains with a large number of annealing twins; (b) enlarged view of the microstructure with (Ti,Nb) carbides visible as small, dark particles (examples indicated by black arrows); (c) CTEM selected area diffraction pattern showing peaks corresponding to the γ matrix, and no peaks corresponding to the ordered γ′ phase.

normal orientation. As in equiatomic CrCoNi and alloy 740H, V1 contained abundant annealing twins (approximately 40% of the total high angle grain boundary length present in Fig. 4a). There was no indication of strong texture and intragranular misorientations were small, indicating full recrystallization. Fig. 4b shows a higher magnification backscattered electron (BSE) image with equiaxed grains. EDS (not shown) indicated that small, dark particles visible in Fig. 4b had compositions consistent with MC-type carbides enriched in Ti and Nb. No other phases were observed at SEM length scales, including γ'. The absence of γ′ and other finer precipitates was also confirmed via TEM. Fig. 4c shows an <001> zone axis conventional transmission electron microscope image of the as-quenched microstructure with an inset selected area diffraction pattern, confirming the lack of γ' reflections.

X-ray diffraction (XRD) results for the fully recrystallized and solutionized condition are shown in Fig. 5a (red curve) with peaks corresponding to a single-phase γ matrix with a face-centered cubic (fcc) structure. The data were fit with a split-Voight function and refined to estimate a lattice parameter $a = 3.59$ Å. As expected, no additional peaks were observed for the γ' or σ phases, nor for the previously observed carbide phase due to its small volume fraction. Weak texture was indicated by the higher integrated intensity of the 200_{fcc} reflection compared to the 111_{fcc} reflection. However, due to the large grain size (~60 μm), this may be a product of sampling a relatively small number of grains.

3.3. Aging results – fully recrystallized material

Grain structures for several aging conditions are shown in Fig. 6. The left column, Fig. 6a–e, corresponds to aging from the fully recrystallized starting condition previously shown in Fig. 4. Like the solutionized and quenched material, these had relatively equiaxed grains and did not exhibit significant grain growth. Both the 700 °C/1 h and 800 °C/1 h conditions had an average grain size of 59 ± 2 μm (essentially identical to the solutionized and quenched specimen), and the 900 °C/1 h condition exhibited very modest growth to an average of 63 ± 2 μm. After longer aging times at 800 °C/100 h and 900 °C/100 h, the apparent grain size slightly decreased to 54 ± 1 μm due to precipitation and growth of additional phases along grain boundaries. These results indicate that no significant grain growth occurs up to at least 900 °C.

XRD results for the 800 °C/100 h condition are shown in Fig. 5a (blue curve) and exhibited low-intensity reflections corresponding to the precipitation of both γ′ and σ phase. The data were fit with a split-Voight function and refined to determine lattice parameters of $a = 3.58$ Å for the γ matrix and $a = 3.60$ Å for the γ' precipitates. The

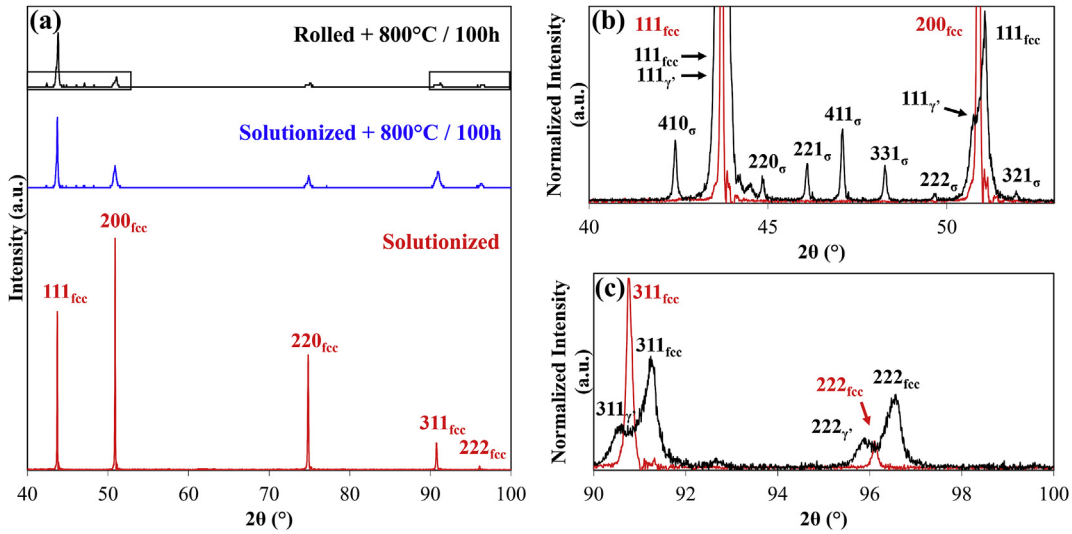

Fig. 5. XRD results from the fully recrystallized and solutionized condition (red); the fully recrystallized, solutionized and aged condition (blue); and the rolled and aged condition (black). (a) Full scan range from 40 to 100° showing reflections for the predominant face-centered cubic structure; (b) inset emphasizing σ phase reflections in the range 40–53°; (c) inset showing splitting of the γ and γ′ peaks after aging 800 °C/100 h from the rolled condition. (For interpretation of the references to color in this figure legend, the reader is referred to the Web version of this article.)

tetragonal σ phase had lattice constants $a = 8.78$ Å, $c = 4.56$ Å. Similar results were also observed for the 900 °C/100 h condition (not shown).

The SEM images of Fig. 7 show the size and distribution of γ′ precipitates following etching, which selectively attacks the γ′ phase to facilitate quantification. The left column, Fig. 7a–e, corresponds to aging from the fully recrystallized starting condition previously shown in Fig. 4. Isochronal annealing produced a range of γ′ sizes spanning from less than 10 nm (700 °C/1 h) to 39 nm (900 °C/1 h). Longer aging treatments resulted in coarsening or Ostwald ripening of the γ'.

Comparison of simulated Thermo-Calc results to the experimental measurements demonstrates close agreement for the area/volume fraction measurements; for example, non-equilibrium Thermo-Calc aging simulations predicted a volume fraction of 0.16 γ' after aging at 900 °C/1 h, compared to an experimental area fraction of 0.16 ± 0.006. Predictions for size were less accurate; at the same aging condition, the predicted diameter was 65 nm, compared to an observed average diameter of 39 ± 0.8 nm. Coarsening rates were dramatically over-predicted at longer aging times, with Thermo-Calc predicting a diameter of 313 nm compared to the observed 138 nm after aging at 900 °C/100 h. The results for aging at 800 °C were similar, with good agreement on area/volume fractions but substantial over-prediction of size.

Precipitation of σ-phase was observed along high-angle grain boundaries, along with directional coarsening of γ' precipitates. Fig. 8 shows higher magnification backscattered electron images highlighting behavior near grain boundaries. Although XRD results from the 800 °C/1 h and 900 °C/1 h conditions exhibit very low-intensity peaks corresponding to the σ-phase (not shown), it is not visible along grain boundaries at such short aging times (Fig. 8a and b). However, precipitation of σ-phase as discrete particles is clear in Fig. 8c and d after aging at 800 °C/100 h and 900 °C/100 h. Although the σ-phase volume fraction was not quantified, there appeared to be less in the 900 °C/100 h condition than after 100 h at 800 °C. No σ-phase was observed along annealing twins or within grains.

Directional coarsening of γ′ precipitates at grain boundaries is highlighted in Fig. 8e–h. Even after aging for a relatively short duration of 1 h, γ′ particles were elongated perpendicular to high angle grain boundaries (HAGBs). At 800 °C/1 h, coarsening occurred even on apparently straight HAGB segments and extended into the grains on both sides of the same boundary (Fig. 8e). Surprisingly, the coarsened regions qualitatively appeared smaller for the 900 °C/1 h condition (Fig. 8f), which is not intuitive since higher temperatures are typically associated with higher coarsening rates. The morphology of the coarsened regions also changed from appearing on both sides of the same boundary (800 °C) to only on one side of a given boundary (900 °C). As indicated in the figure, some regions along the coarsened boundaries were also denuded of γ' directly adjacent to coarsened particles.

Longer aging times increased the size of the coarsened regions, although the morphology of the 900 °C/100 h condition (Fig. 8h) remained the same and coarsened regions were not dramatically larger than the 900 °C/1 h condition. In contrast, the regions near HAGBs experienced considerable additional coarsening after 800 °C/100 h, in addition to which the HAGBs became extremely tortuous with interlocking coarsened regions (see example in Fig. 8g). For both longer aging conditions, σ-phase was also observed in and around regions with coarsened γ', further complicating the boundary structure.

3.4. Aging response – rolled material

In addition to aging the alloy from a fully recrystallized state, aging was performed following a 70% reduction in thickness by cold-rolling to examine the influence of prior deformation. Grain structures for the rolled and aged material are shown in the right column of Fig. 6, Fig. 6f–j. These remained highly deformed following rolling and aging and had grains aligned with the rolling direction (the vertical direction in the page). There was no indication of recrystallization in the 700 °C/1 h or 800 °C/1 h conditions, whereas only limited recrystallization occurred after 900 °C/1 h and 800 °C/100 h. Substantial recrystallization occurred after 900 °C/100 h. Quantification of the recrystallized volume fraction is problematic due to the large scale heterogeneity of the microstructure, which contained roughly linear bands of recrystallized grains separated by distances ranging from dozens of microns to several millimeters.

As in the recrystallized and aged material, XRD results indicated

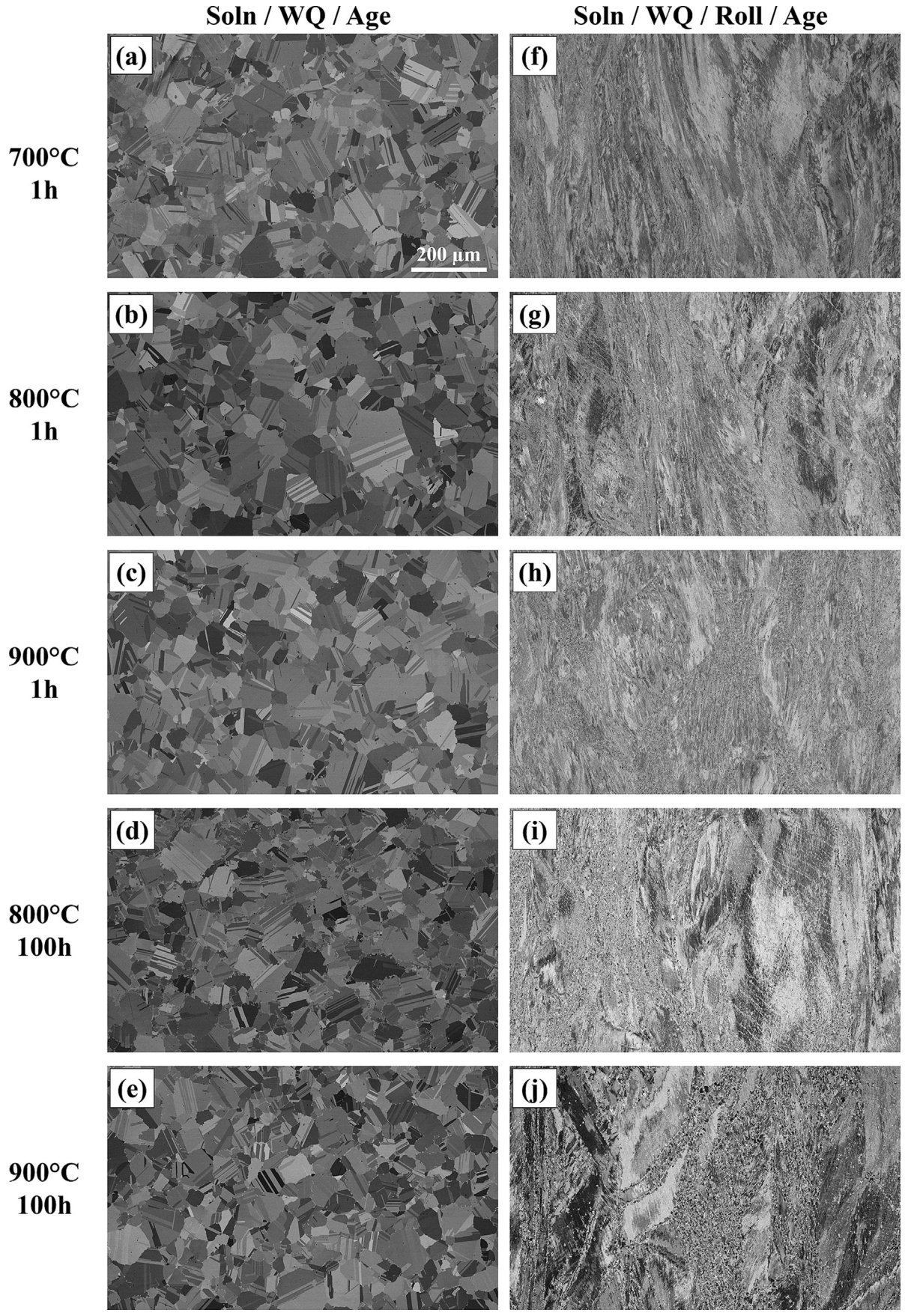

Fig. 6. Grain structures following aging treatments for the fully recrystallized (left) and rolled conditions (right). All images were acquired at the same magnification and working distance.

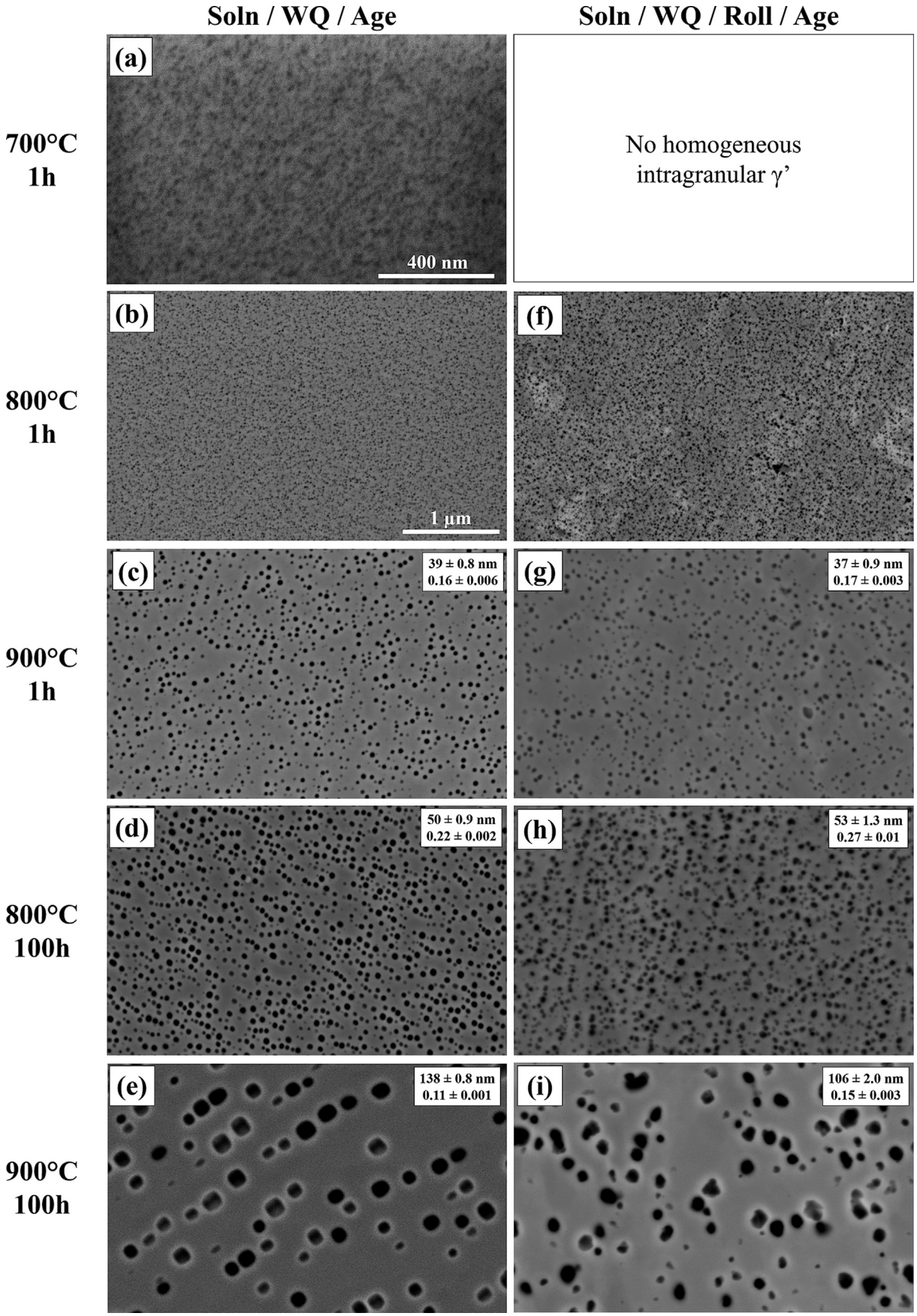

Fig. 7. Etched specimens showing γ′ after aging treatments for the fully recrystallized (left) and rolled conditions (right). All images were acquired at the same magnification and working distance, except the 700 °C/1 h condition due to the extremely fine precipitates. Precipitate diameter and volume fraction are indicated in the top right corners of (c)–(i).

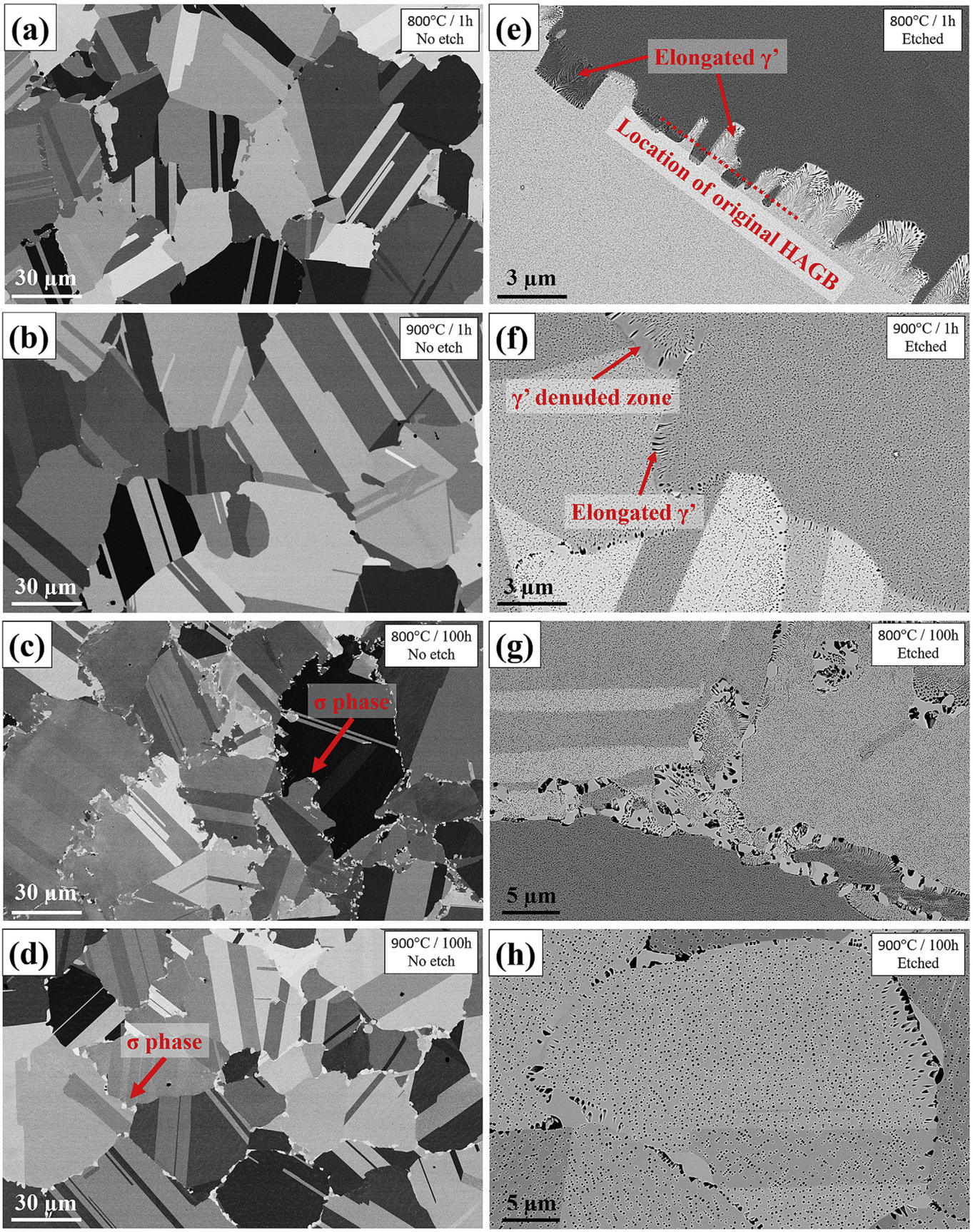

Fig. 8. Grain boundary behavior after aging in the fully recrystallized condition. BSE images in the left column show precipitation of discrete σ phase along boundaries after long aging times; BSE images in the right column images show directional coarsening of γ′ at grain boundaries.

precipitation of γ′ and σ phase. Fig. 5a shows a diffractogram for the rolled and aged 800 °C/100 h condition over the 2θ range 40°–100° (black curve) with boxes indicating the domain for the inset regions in Fig. 5b and c. Fig. 5b shows the most prominent σ phase reflections between 2θ values of approximately 40° and 53°, while splitting of the γ' and γ matrix peaks was clearly observed at larger 2θ values between 90° and 100° in Fig. 5c.

Specimens were etched to facilitate measurement of γ′ precipitates with results shown in Fig. 7. Unlike the fully recrystallized material, the rolled material exhibited two distinct populations of γ′ with substantial differences between recrystallized and non-recrystallized regions. These are illustrated in Fig. 9b, which shows fine γ′ in the non-recrystallized grains and coarse γ′ along HAGBs between recrystallized grains. Although the precise formation mechanism of the coarse γ' is unknown, it is likely related to transport of Al and Ti along HAGBs during recrystallization. The images in Fig. 7 corresponding to the rolled and aged material (Fig. 7f–i) were all acquired exclusively in non-recrystallized regions, and it is important to note that subsequent discussion of this figure does not apply to recrystallized regions.

Surprisingly, no uniform precipitation of intragranular γ′ was observed in the rolled/700 °C/1 h condition. Intragranular γ′ was instead observed in directionally coarsened regions adjacent to slip bands, unlike in any of the fully recrystallized conditions. Like the recrystallized material, however, the rolled and aged condition also had directionally coarsened γ' along high angle grain boundaries.

The other aging conditions for the rolled material produced very similar γ′ distributions compared to the recrystallized and aged material. For example, after aging at 900 °C/1 h, the fully recrystallized and aged material had an average γ′ diameter of 39 nm with an area fraction of 0.16 (Fig. 7c); the rolled material had an average γ′ diameter of 37 nm with an area fraction of 0.17 (Fig. 7g). Some discrepancy was observed for the 900 °C/100 h condition, with the rolled material exhibiting smaller γ' than the recrystallized material (106 nm compared to 138 nm). Although many of the precipitates in this condition are no longer spherical, they do not exhibit a clear cuboidal morphology like the corresponding fully recrystallized material.

Fig. 9 shows intermediate magnification images of the rolled/800 °C/100 h condition. EDS chemical mapping in Fig. 9a shows three distinct phases in addition to the background γ matrix. First, there are regions enriched in both Ni and Ti that correspond to coarse γ'. As previously noted, these precipitates form primarily along HAGBs between recrystallized grains and are shown in more detail in Fig. 9b. Note that these are distinct in size and morphology from the much finer precipitates in non-recrystallized regions previously shown in Fig. 7. HAGBs were also decorated by σ-phase, which is enriched in Cr. The final phase shown in Fig. 9, which does not appear in XRD results due to its small volume fraction, is TiC. These particles are highly enriched in Ti relative to both the γ matrix and γ′ precipitates and can be clearly observed on the Ti map. Fig. 9b shows a similar region in greater detail with clear distinctions visible between coarse and fine γ'. Unlike the fully recrystallized material, some σ-phase was observed away from grain boundaries and is marked on the image.

EBSD and EDS were used to more clearly demonstrate the intragranular nucleation of σ-phase, as shown in Fig. 10 for the rolled/800 °C/100 h condition. Fig. 10a shows an inverse pole figure (IPF) map near a high angle grain boundary with color denoting crystallographic orientation. Several isolated recrystallized grains were observed along the original HAGB and within the upper grain (as denoted by local regions with different orientations); however, most of the surveyed region remained non-recrystallized and highly deformed, as indicated by orientation (color) gradients within individual grains. Fig. 10b shows a phase map, also produced by EBSD, differentiating between the cubic structure of the γ matrix and γ' precipitates (red), and the tetragonal structure of σ-phase (green). These results are corroborated by EDS from the same region, Fig. 10c, which shows corresponding enrichment of chromium in the same areas. An additional example of planar σ-phase nucleation is shown for the rolled/800 °C/100 h condition in Fig. 10d and e.

Unlike the fully recrystallized material, σ-phase formation is shown within intragranular regions. Precipitation is predominantly planar and most likely associated with {111} slip planes with high initial dislocation densities following rolling. Although γ' is not indicated on the EBSD maps, it can be differentiated on the EDS maps by regions enriched in Ni, Al, Ti, and Nb.

3.5. Hardness evolution with aging

Vickers microhardness was measured as a function of aging temperature and time. Fig. 11a shows the results of isochronal (1 h) aging at different temperatures, for both fully recrystallized (blue curve) and rolled (black curve) alloy conditions. Bars on the measurements show the full spread of values for each condition to emphasize the variability in the rolled material.

The fully recrystallized material exhibited a classic aging response for a precipitation-hardened alloy. The hardness increased with increasing temperature from 500 °C to 800 °C as the

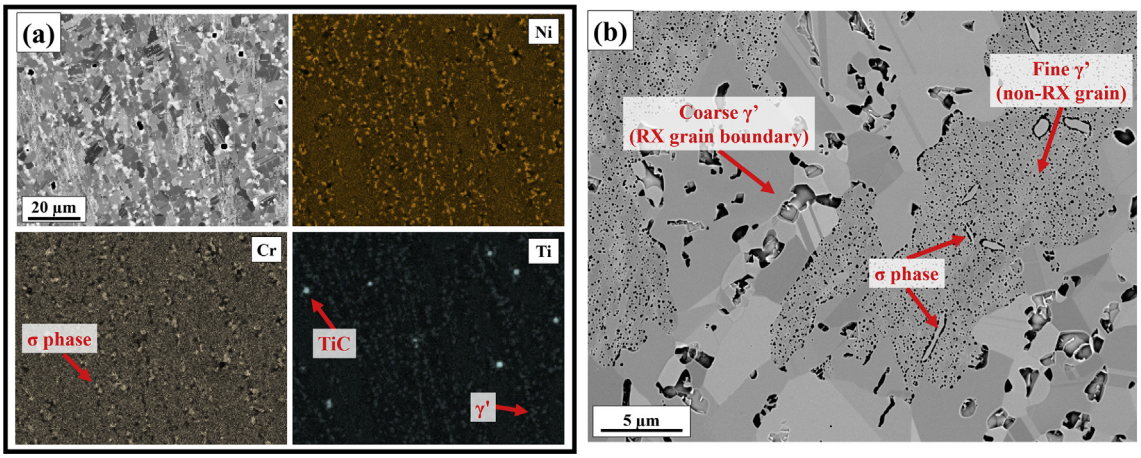

Fig. 9. (a) Development of σ phase along high angle grain boundaries and {111} planes in rolled and annealed material (800 °C/100 h), and (b) γ′ phase in recrystallized and non-recrystallized regions.

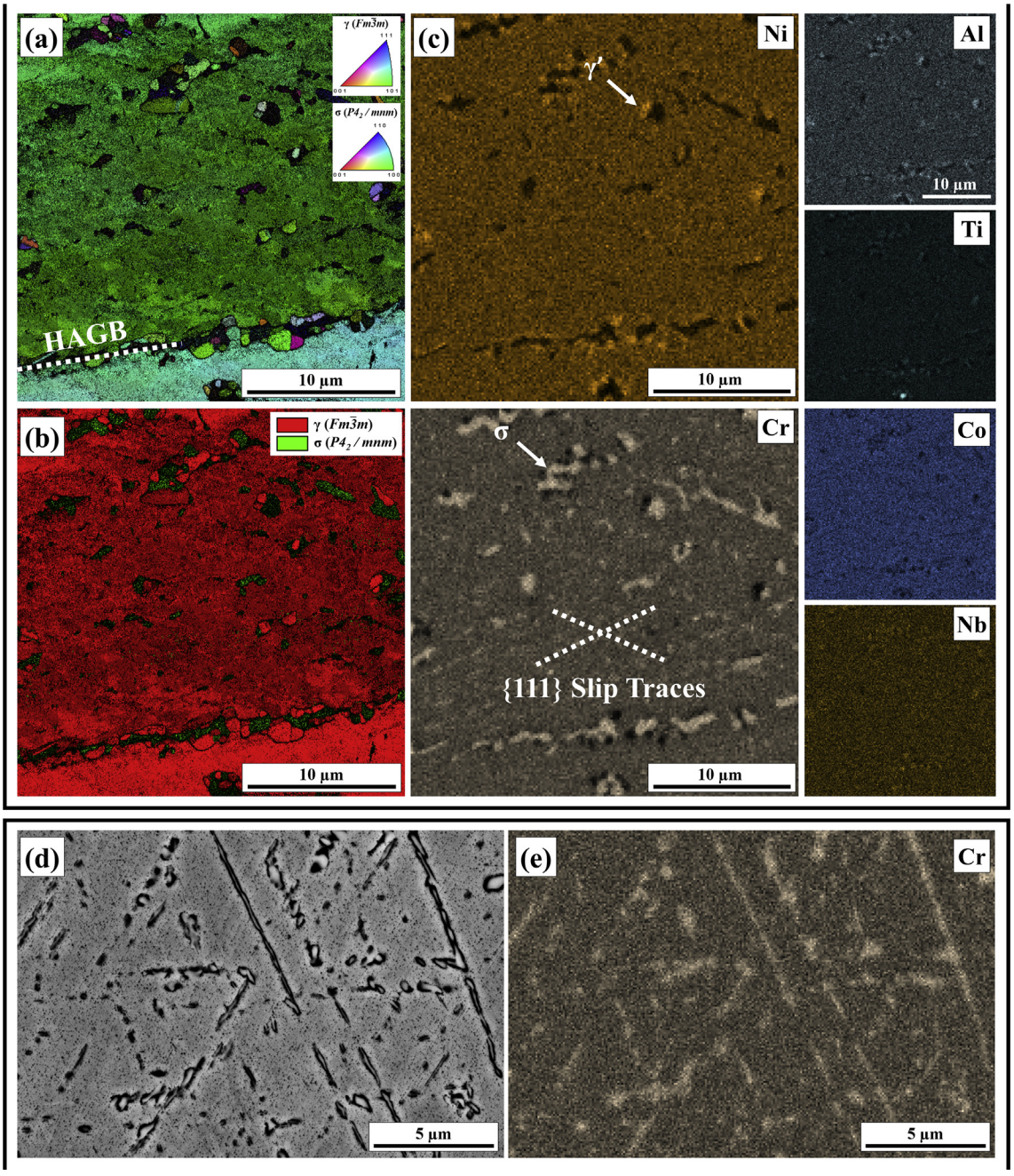

Fig. 10. Development of σ phase along high angle grain boundaries and {111} planes in rolled and annealed material (800 °C/100 h). (a) IPF map showing grain orientations; (b) EBSD result showing location of γ/γ′ and σ phase based on structure; (c) EDS results from the same region indicating enrichment of Cr in σ phase. An additional example of planar σ-phase nucleation is shown using in-column BSE imaging, (d) and SEM-EDS mapping of the same region, (e).

volume fraction and size of γ' precipitates increased. The peak average hardness, 392 ± 10 HV (standard deviation), was reached at 800 °C, and represents a 58% increase over the solutionized and quenched condition (248 ± 7 HV, blue hatched band). Based on the average grain size (~60 μm) and the typical microhardness indent size (~20 μm), it is likely that some variability arose from sampling within single grains.

The rolled condition exhibited substantially higher hardness values. The average hardness of the as-rolled material, 504 ± 26 HV (black hatched band), was more than double that of the fully recrystallized material. Note that the as-rolled material had previously been solutionized and quenched, and therefore is not strengthened by precipitates. The aging response was otherwise similar to the fully recrystallized material, with an initial increase in hardness up to a peak of 614 ± 48 HV at 700 °C/1 h. Despite the higher strengthening contribution from precipitation at 800 °C, the total hardness began decreasing at 700 °C due to more substantial recovery and possibly the beginning of recrystallization. As previously noted, recrystallization was clearly observed via SEM after 900 °C/1 h, which was reflected in the lower hardness measurement. Fig. 11b compares the hardness evolution in the rolled alloy to that in CrCoNi with an identical rolling reduction, which has previously been reported by Slone et al. [40]. In addition to having a higher peak hardness, alloy V1 retains its high hardness levels after

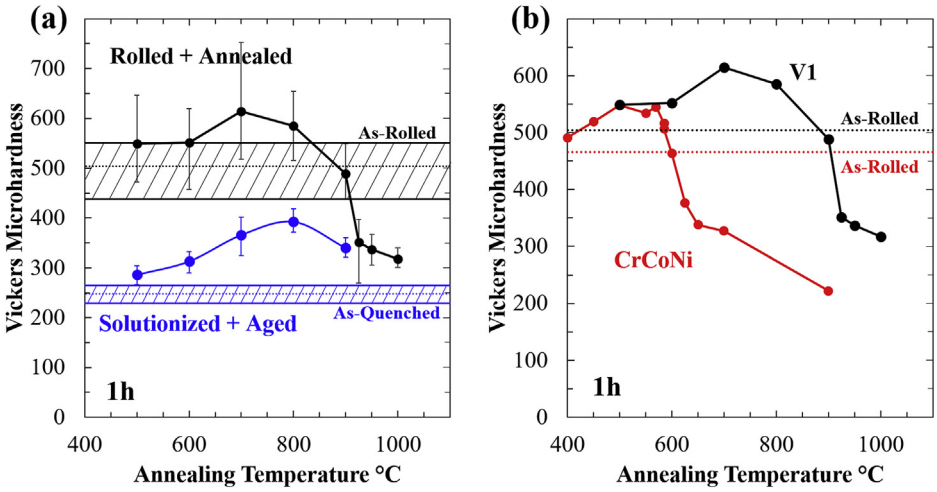

Fig. 11. Hardness evolution in alloy V1 as a function of temperature for 1 h isochronal aging treatments. (a) Comparison of the aging response in the fully recrystallized (blue) and rolled (black) conditions. Hatched bands show the range of hardness values for as-rolled and as-quenched conditions. (b) Comparison of the response in precipitation-hardened V1 (black) to solid solution, equiatomic CrCoNi (red). (For interpretation of the references to color in this figure legend, the reader is referred to the Web version of this article.)

annealing at much higher temperatures. This indicates a delay in recrystallization (i.e. higher temperatures required), likely caused by the presence and pinning effect of γ' precipitates.

4. Discussion

The new alloy described in the present work was inspired by medium-entropy, equiatomic CrCoNi and commercial Ni-base superalloy Inconel 740H. There is a natural congruity between these two alloys resulting from their large nickel, chromium, and cobalt contents; however, the rolling response and microstructure evolution of the new alloy, V1, shares more in common with previous observations of alloy 740H than equiatomic CrCoNi. This is reflected in the nucleation and growth of γ' precipitates; directional coarsening of precipitates along grain boundaries; and the lack of deformation twinning in rolled material. Each of these phenomena are discussed below, in addition to the surprising precipitation of σ phase, which is not present in either parent alloy. Examination of the aging response of the new alloy in the rolled state is especially insightful since this condition is not frequently studied for precipitation-strengthened materials.

4.1. Precipitation of σ phase

Precipitation of σ phase is generally considered problematic in Ni-base superalloys and stainless steels and has been correlated with reduced creep rupture life during loading at elevated temperatures [26,47]. As a topologically close-packed (TCP) phase, σ has extremely limited capacity for plastic deformation and usually embrittles alloys as a continuous phase along HAGBs. Furthermore, σ is Cr-rich and therefore depletes chromium from the alloy matrix, which locally decreases solid solution strengthening and increases susceptibility to intergranular corrosion.

Despite these issues in conventional alloys, precipitation of σ phase as discrete particles may be less harmful in new alloy V1 due to the large overall chromium content in the alloy. For example, Thermo-Calc results suggest the matrix should retain more than 28 at% (25 wt%) chromium even after σ precipitation at temperatures above 700 °C (see Fig. 1), which is greater than the overall chromium content in alloy 740H. This is expected to be more than adequate for even highly corrosive environments [48] and still represents a significant addition for solid solution strengthening. However, it is unclear whether the discrete σ phase precipitates along the boundaries (e.g, Fig. 8d) will deleteriously affect overall alloy ductility, and additionally, whether the reduction of chromium in the matrix phase meaningfully reduces strength. Precipitation of discrete σ particles on HAGBs may even offer some benefit as an impediment to grain growth or grain boundary sliding.

Although large chromium additions are known to induce σ phase precipitation in stainless steels and Ni-base superalloys, it has not been reported following heat treatments in equiatomic CrCoNi (~30.6 wt% chromium), even in conjunction with severe plastic deformation generated by cold-rolling or high-pressure torsion [40,50–54]. One caveat for these studies is that they nearly all use annealing temperatures in the range 500–1000 °C for relatively short times, typically ~1 h. This may be inadequate for σ phase precipitation, although similar temperatures and durations produced σ phase in related CrMnFeCoNi high-entropy alloys [55]. Long-term aging of alloy 740H at a variety of temperatures has also failed to produce σ phase [56], although this alloy notably contains less chromium than either equiatomic CrCoNi or the new alloy from the present work.

It is not immediately clear why σ phase precipitates in alloy V1 but not in either of the parent alloys, equiatomic CrCoNi and alloy 740H; Thermo-Calc predicts σ phase formation in all three, albeit at lower temperatures in CrCoNi and 740H, which may make it kinetically inaccessible in the latter two. Tsai et al. recently examined Cr-containing high-entropy alloys and explained the propensity for σ phase formation using the valence electron concentration (VEC) criterion [57]. VEC for an alloy is defined as the molar composition-weighted average of VEC values for individual elements, which are listed by Guo et al. for a number of commonly used metals [58]. In the work by Tsai et al., alloys with average VECs between 6.88 and 7.84 were σ-prone, while alloys with VECs outside that range were σ-free. Calculation of VEC for alloy V1 suggests that its composition is very close to the threshold (7.98), while equiatomic CrCoNi (8.34) and alloy 740H (8.38) both exceed the threshold range. Table 2 lists the composition and VEC values for each alloy.

The VEC for V1 is lower than for CrCoNi due to additions of aluminum (elemental VEC = 3) and titanium (VEC = 4), and lower than for 740H due to substitution of cobalt (VEC = 9) and especially chromium (VEC = 6) for nickel (VEC = 10). New analysis for the

Table 2
Valence electron concentration (VEC) calculations for alloy V1 and its parent alloys.

		Nominal Alloy Compositions (at%)		
Element	VEC	CrCoNi	IN740H	V1
Ni	10	0.334	0.482	0.310
Cr	6	0.333	0.266	0.311
Co	9	0.333	0.194	0.306
Al	3	-	0.030	0.041
Ti	4	-	0.017	0.023
Nb	5	-	0.009	0.009
Mo	6	-	0.002	-
Weighted Average VEC		8.335	8.377	7.980

present study suggests the VEC criterion for σ phase formation also applies successfully to similar CrMnFeCoNi high-entropy alloys, where $Cr_{26}Mn_{20}Fe_{20}Co_{20}Ni_{14}$ (VEC = 7.76) readily precipitates σ phase [55], and equiatomic CrMnFeCoNi (VEC = 8.0) precipitates σ phase after long anneals or annealing following severe plastic deformation [21,22]. Finally, the VEC criterion also correctly predicts the formation of σ phase in compositionally complex modern superalloys like ME3 (VEC = 7.94), which also forms discrete particles along grain boundaries [59]. The observations from the present work are consistent with the use of the VEC criterion for predicting whether σ phase precipitation will occur.

4.2. Directional coarsening of γ' precipitates

Another key similarity between the new V1 alloy and alloy 740H is the development of elongated γ′ precipitates at, and extending outward from, high angle grain boundaries (HAGBs). This phenomenon has previously been observed in other polycrystalline superalloys [60–63], including 740H [64,65] and equivalent alloys [65,66]. For undeformed material (e.g, the fully recrystallized conditions in Fig. 8), previously suggested mechanisms such as Nabarro-Herring creep and grain boundary sliding [67] are dismissed because they depend on simultaneous exposure to high temperature and an applied load. Precipitate-free zones have also been hypothesized to develop due to formation of Cr-rich carbides [61] or Cr-rich σ phase along HAGBs, which locally deplete chromium and raise the solubility of γ′-forming elements in the matrix. This results in dissolution of the γ′ phase near HAGBs. Although these mechanisms are plausible for alloy V1, given the observed precipitation of σ phase, both are expected to produce symmetrical precipitate-free zones along grain boundaries, particularly near Cr-rich particles. This is not consistent with the asymmetric regions observed in Fig. 8e– h.

Bechetti et al. previously identified directional or discontinuous coarsening as the formation mechanism for elongated γ′ in alloy 740H [64]. This mechanism is well-known and has been studied in a variety of other systems with strengthening particles, most notably Al-Li [68]. The asymmetric, elongated precipitate morphology in alloy V1 is consistent with discontinuous coarsening, although it is not clear from the current work whether elongated γ' forms by discontinuous precipitation along the boundary or forms homogeneously and then undergoes discontinuous coarsening.

In either case, the morphology at 800 °C (Fig. 8e) does not suggest that coarsening is driven by grain growth, since coarsened precipitates have extended from both sides of a HAGB into separate grains. This morphology was common after short-duration aging at 800 °C and is reminiscent of the "S-mechanism" originally described by Fournelle [69] and reviewed for a wide variety of alloy systems by Williams and Butler [68]. Further support for this development mechanism can be seen in the lower right corner of Fig. 8g, which shows a classic "double-seam" boundary after extended aging at 800 °C.

Directionally coarsened particles occurred much more commonly along only one side of HAGBs after aging at 900 °C, in contrast to the behavior at 800 °C. Given that very modest grain growth was observed at the higher temperature, unlike at lower temperatures where grain growth was not observed, it is possible the change in morphology was due to grain growth and solute drag with the boundary rather than the S-mechanism described above. A mechanism change is also consistent with the lesser extent of directional coarsening after 100 h at 900 °C (Fig. 8h) compared to 800 °C (Fig. 8g), which is otherwise surprising since the higher temperature and faster kinetics would usually be expected to promote greater coarsening. Further discussion of the driving force and origin of directionally-coarsened precipitates follows in the next section.

4.3. Comparison of fully recrystallized and rolled material

Intragranular γ' precipitate distributions were similar in the fully recrystallized and rolled conditions following aging at 800 °C and 900 °C, but not at 650 °C and 700 °C. This effect can be ascribed to differences in the relative contribution of grain boundaries, dislocations, and the matrix to the overall diffusion rate. The interpretation discussed below is summarized in Table 3 with a qualitative comparison of the volume fraction *f* and diffusion coefficient *D* for grain boundaries (gb), dislocations (disl), and the matrix (M).

All material was initially homogenized at temperatures above the γ′ solvus and quenched before undergoing additional aging or rolling and aging. Since γ′ is an equilibrium phase at room

Table 3
Summary and interpretation of precipitate nucleation and growth. The interpretation refers to the relative contributions from grain boundaries (gb), dislocations (disl), and the matrix (M) to γ' precipitation. The contribution of each is the product of its volume fraction *f* and its diffusion coefficient *D*.

Aging Condition	~ T/T_m	γ′ in Solutionized + Aged Condition	γ′ in Solutionized + Rolled + Aged Condition	Interpretation
650 °C/4 h	0.51	No apparent homogeneous precipitation within grains; severe discontinuous coarsening at HAGBs	No apparent homogeneous precipitation within grains; severe discontinuous coarsening at HAGBs; isolated precipitation along intragranular slip bands	$f_{gb}D_{gb} > f_{disl}D_{disl} \gg f_MD_M$
700 °C/1 h	0.55	Very fine homogeneous precipitation within grains; severe discontinuous coarsening at HAGBs	No apparent homogeneous precipitation within grains; severe discontinuous coarsening at HAGBs; modest discontinuous coarsening along intragranular slip bands	$f_{gb}D_{gb} > f_{disl}D_{disl} > f_MD_M$
800 °C/1 h	0.63	Fine homogeneous precipitation within grains; modest discontinuous coarsening at HAGBs	No significant difference from Solutionized + Aged condition	$f_{gb}D_{gb} > f_MD_M \sim f_{disl}D_{disl}$
900 °C/1 h	0.70	Coarse homogeneous precipitation within grains; mild discontinuous coarsening at HAGBs	No significant difference from Solutionized + Aged condition	$f_{gb}D_{gb} >\sim f_MD_M \gg f_{disl}D_{disl}$
960 °C/1 h	0.75	Coarse homogeneous precipitation within grains; very mild or negligible discontinuous coarsening at HAGBs	No significant difference from Solutionized + Aged condition	$f_{gb}D_{gb} \sim f_MD_M \gg f_{disl}D_{disl}$

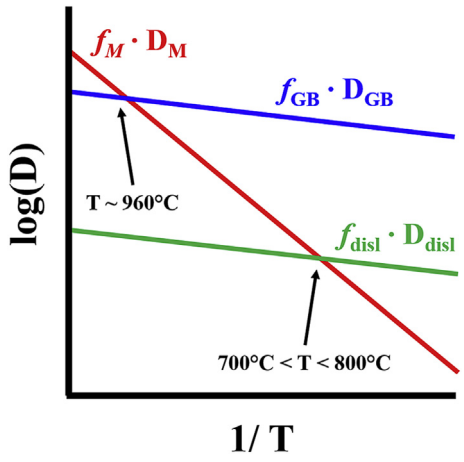

Fig. 12. Schematic illustration of how temperature affects diffusion at high angle grain boundaries, dislocations, and the bulk matrix. At low temperatures, diffusion is more prevalent along grain boundaries and dislocations despite their small relative volume; at high temperatures, diffusion in the matrix dominates.

temperature, the matrix after quenching is supersaturated with γ′-forming elements aluminum and titanium. The supersaturation provides a strong driving force for precipitation, but the diffusion required is inhibited at low temperatures. It is well-known that the additional free volume associated with high angle grain boundaries and dislocations enables faster local diffusion relative to the bulk matrix. This promotes precipitation along grain boundaries, particularly at lower temperatures. However, the effect scales strongly with temperature because the absolute volume of grain boundaries and dislocations is small in comparison to that of the matrix. At higher temperatures, when diffusion through the matrix becomes fast, the product of the diffusion coefficient and the effective diffusion volume overwhelms the contribution from grain boundaries or dislocations. This is schematically illustrated in Fig. 12.

The practical implications for this in the current alloy are reflected in the γ′ morphology and distributions across different temperatures. Fig. 13 shows several additional micrographs to emphasize the differences. For the lowest temperatures (650 °C and 700 °C), matrix diffusion is extremely slow since the homologous temperatures $T/T_{solidus}$ are approximately 0.51 and 0.55, respectively, using $T_{solidus} = 1277$ °C from Thermo-Calc. Diffusion along grain boundaries and dislocations is therefore expected to dominate over diffusion through the matrix. For the fully recrystallized material, where the dislocation density is low, no homogeneous intragranular γ' precipitation was observed even after 4 h at 650 °C.

Fig. 13a shows that this condition also exhibited the most severe directional coarsening at high angle grain boundaries, suggesting that supersaturation of γ′-forming elements was relieved exclusively along fast diffusion pathways. It should be noted that grain boundary coarsening was most severe at this low temperature despite also having the slowest kinetics, further emphasizing the importance of internal boundaries. In the corresponding rolled and aged condition, some intragranular precipitation was observed in regions of high dislocation density along slip bands (Fig. 13d) in addition to directionally coarsened particles along grain boundaries (Fig. 13c).

Increasing the aging temperature promoted the importance of matrix diffusion at the expense of diffusion along dislocations and, at longer aging times, grain boundaries. Aging at 700 °C/1 h from the fully recrystallized state indicated that matrix diffusion was sufficiently fast to precipitate homogeneous, intragranular precipitates (Fig. 7a), although no homogeneously distributed precipitates were observed in the corresponding rolled condition because diffusion and precipitation at dislocations was still preferred. At 800 °C and 900 °C, the increasing matrix diffusion rate and its larger overall volume combined to promote greater flux through the matrix than along dislocations. The fully recrystallized and rolled conditions therefore look similar (Fig. 7b and f, Fig. 7c and g) since supersaturation of γ′-forming elements can easily be relieved by matrix diffusion alone.

Although directional coarsening of γ' was still observed at 800 °C and 900 °C ($T/T_{solidus} = 0.63$ and 0.70, respectively), the extent of the coarsening decreased with increasing temperature.

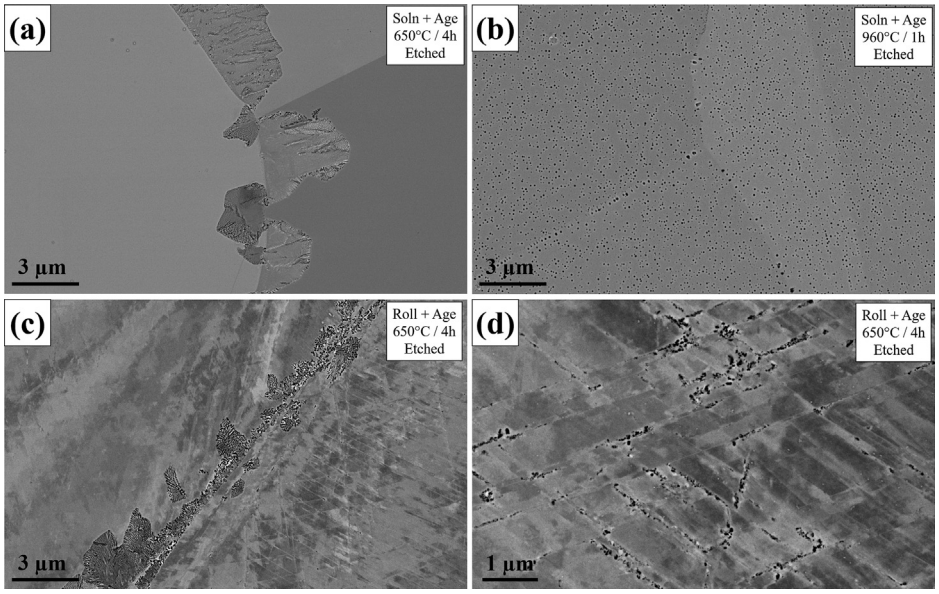

Fig. 13. Changes to the interaction of γ′ with high angle grain boundaries at 650 °C and 960 °C. (a) Severe directional coarsening in the fully recrystallized material after aging 650 °C/4 h; (b) absence of coarsening in the fully recrystallized material after aging 960 °C/1 h; (c) directional coarsening from HAGBs in the cold-rolled material after aging 650 °C/4 h; (d) heterogeneous precipitation of γ′ on dislocation bands in the cold-rolled material after aging 650 °C/4 h.

This suggests that grain boundary diffusion remains important in relieving supersaturation at those temperatures. However, increasing the temperature further to 960 °C ($T/T_{solidus} = 0.75$) eliminated directional coarsening almost entirely (Fig. 13b) as the effective diffusion rate in the matrix achieved parity with that along grain boundaries. Some isolated instances of very fine directional coarsening were observed; but most boundaries looked like those in Fig. 13b which showed only slightly enlarged precipitates with no indication of growth perpendicular to grain boundaries.

These observations may prove to be important not only for the present alloy, but also alloys like 740H, where discontinuous coarsening at boundaries is problematic for high-temperature creep properties [63]. Alloy 740H and other polycrystalline alloys with this issue are currently aged at temperatures around 800 °C, which seems to be a highly susceptible temperature based on the present study. The current results suggest that coarsening could be avoided by aging at higher temperatures (to promote the importance of matrix diffusion at the expense of grain boundary diffusion); however, doing so reduces the equilibrium volume fraction of γ'. Increasing the concentrations of γ′-forming elements might offset this by increasing the equilibrium γ′ volume fraction at, for example, 960 °C. It is unlikely that this is an industrially acceptable solution since doing so also makes alloys very challenging to weld. One possible compromise might involve small compositional changes (increase in γ′-forming elements) coupled with processing changes including a furnace cool from the solutionizing to aging temperatures. In that case, matrix supersaturation can be initially relieved at higher temperatures where matrix diffusion dominates.

It should also be noted that this effect may be exacerbated by the hypothesized "sluggish diffusion" mechanism in multi-principal element alloys, which has been experimentally observed in the equiatomic CrMnFeCoNi alloy [10]. Although sluggish diffusion is usually considered to be a positive effect for producing stable, creep-resistant microstructures, it may be a disadvantage during aging in highly concentrated superalloys like 740H if it hinders matrix diffusion and promotes discontinuous coarsening via diffusion along grain boundaries.

4.4. Absence of deformation twinning after rolling

Although the mechanical response and deformation mechanisms in alloy V1 are being investigated in a separate study, it is worth noting here that no evidence was observed for deformation twinning following cold-rolling. Deformation twinning is commonly observed after rolling or high-pressure torsion in equiatomic CrCoNi [40,50–54] but not in solutionized/quenched 740H [44]. While transmission electron microscopy methods were not used specifically to search for evidence of deformation twinning in the current work, experience with previous alloys has shown that twins are readily visible using high spatial resolution EBSD or electron channeling contrast imaging, both of which were employed here.

It was previously speculated that average stacking fault energy (SFE) might explain the discrepancy between CrCoNi and 740H [44], since low SFE promotes dislocation dissociation and has been consistently correlated with deformation twinning in fcc alloys [70]. Although elemental nickel has a relatively high SFE (~150 mJ/m^2), it is well-known in the superalloys literature that chromium and cobalt dramatically reduce it. The experimentally measured SFE in CrCoNi is approximately 22 mJ/m^2 [38] to 18 mJ/m^2 [71], compared to an estimate from software JMatPro [72] of 45 mJ/m^2 in alloy 740H (which contains less Cr and Co and, therefore, should have a higher SFE). Deformation twinning in face-centered cubic (fcc) alloys is usually associated with average SFE values of 40–45 mJ/m^2 or less [70], so the larger value in 740H could plausibly explain why no deformation twinning was observed.

However, the new V1 alloy should have an average SFE similar to that of equiatomic CrCoNi. Although Al and Ti undoubtedly affect the average SFE, they have opposite tendencies (Al increases SFE in Ni-base alloys while Ti decreases SFE) and are present in relatively small quantities (~6 at% combined for both elements) [73,74]. Even if Al alone makes up about 6 at% of the alloy, a simple linear mixture of SFE values for $(CrCoNi)_{94}Al_6$ suggests an average SFE of ~29 mJ/m^2. Although this is a highly simplified estimate, it is unlikely that Al sufficiently raises the average stacking fault energy to entirely deactivate the deformation twinning mechanism, especially given that other HEAs have exhibited twinning with similar and larger SFEs around 40 mJ/m^2 [71]. Alloy V1 also exhibited a very high fraction of annealing twin boundaries (~40% of total HAGB length) in the solutionized and quenched condition, further indicating low SFE. One possible alternative explanation is that γ′-forming elements (Al and Ti) are not randomly distributed in solution. Although diffraction patterns of the solutionized and quenched material (i.e, the condition immediately prior to rolling) did not exhibit reflections corresponding to the ordered γ′ phase (Fig. 4), Al and Ti atoms might have chemically clustered without ordering in a spinodal-type reaction as a precursor to fully-ordered γ'. However, a full exploration of deformation mechanisms in the new V1 alloy is beyond the scope of the present work and is being separately investigated.

5. Conclusions

A new alloy was developed combining aspects of the medium-entropy CrCoNi alloy with Ni-base superalloy Inconel 740H. The alloy was aged from two conditions, fully recrystallized and cold-rolled, to study precipitation with and without prior deformation. The following conclusions can be derived from the present work:

1. Solutionizing and quenching the new V1 alloy produced a predominantly single-phase, face-centered cubic microstructure with infrequent (Ti,Nb) carbides and an average grain size of ~60 μm.
2. Aging at temperatures between 700 and 900 °C resulted in precipitation of γ′ and σ phases. The average grain diameter remained stable even after the most extreme observed condition, 100 h at 900 °C.
3. Fully recrystallized conditions had homogeneous, spherical γ′ precipitates within grains and directionally coarsened particles at grain boundaries. The morphology of the directionally coarsened precipitates appeared to change between 800 °C and 900 °C, which may reflect a change in growth mechanism. After long aging times, σ phase was visible as discrete particles along grain boundaries.
4. Cold-rolled and aged alloys had heterogeneous, partially recrystallized microstructures after aging at sufficiently high temperatures or long times. Non-recrystallized grains had homogeneous γ′ distributions matching those after aging in the non-rolled material; recrystallized grains were usually denuded of γ′ in their interiors and decorated by coarse γ′ along grain boundaries. σ phase precipitated along boundaries between recrystallized grains and along {111} slip traces in non-recrystallized grains.
5. Discontinuous coarsening of γ′ along grain boundaries results from differences in diffusion rates along grain boundaries, dislocations, and the matrix. Coarsening can be eliminated by aging at sufficiently high temperatures where matrix diffusion dominates.
6. Formation of σ phase in this alloy, and absence of σ phase in similar parent alloys CrCoNi and 740H, was consistent with

previous applications of the valence electron concentration (VEC) criterion.

7. Unlike equiatomic CrCoNi, new alloy V1 did not exhibit indications of deformation twinning following cold-rolling. This is unlikely to be an effect of stacking fault energy alone and is being investigated separately, along with the mechanical properties and deformation mechanisms for this alloy.

Declaration of competing interest

The authors declare that they have no known competing financial interests or personal relationships that could have appeared to influence the work reported in this paper.

Acknowledgments

The National Science Foundation, Division of Materials Research is acknowledged for supporting CES and MJM (thermo-mechanical processing and materials characterization) under contract DMR-1508505 and DMR-1905748. CES was also supported by the National Science Foundation Graduate Research Fellowship Program Grant No. DGE-1343012. Any opinions, findings, and conclusions or recommendations expressed in this material are those of the authors and do not necessarily reflect the views of the National Science Foundation. The U.S. Department of Energy, Office of Science, Basic Energy Sciences, Materials Sciences and Engineering Division is acknowledged for supporting EPG (materials synthesis).

References

[1] A. Gali, E.P. George, Tensile properties of high- and medium-entropy alloys, Intermetallics 39 (2013) 74–78, https://doi.org/10.1016/j.intermet.2013.03.018.
[2] B. Gludovatz, A. Hohenwarter, D. Catoor, E.H. Chang, E.P. George, R.O. Ritchie, A fracture-resistant high-entropy alloy for cryogenic applications, Science (80-.) 345 (2014) 1153–1158, https://doi.org/10.1126/science.1254581.
[3] D.B. Miracle, J.D. Miller, O.N. Senkov, C. Woodward, M.D. Uchic, J. Tiley, Exploration and development of high entropy alloys for structural applications, Entropy 16 (2014) 494–525, https://doi.org/10.3390/e16010494.
[4] Z. Li, K.G. Pradeep, Y. Deng, D. Raabe, C.C. Tasan, Metastable high-entropy dual-phase alloys overcome the strength–ductility trade-off, Nature 534 (2016) 227, https://doi.org/10.1038/nature17981.
[5] B. Gludovatz, A. Hohenwarter, K.V.S. Thurston, H. Bei, Z. Wu, E.P. George, R.O. Ritchie, Exceptional damage-tolerance of a medium-entropy alloy CrCoNi at cryogenic temperatures, Nat. Commun. 7 (2016) 10602, https://doi.org/10.1038/ncomms10602.
[6] D.B. Miracle, O.N. Senkov, A critical review of high entropy alloys and related concepts, Acta Mater. 122 (2017) 448–511, https://doi.org/10.1016/j.actamat.2016.08.081.
[7] F. Otto, Y. Yang, H. Bei, E.P. George, Relative effects of enthalpy and entropy on the phase stability of equiatomic high-entropy alloys, Acta Mater. 61 (2013) 2628–2638, https://doi.org/10.1016/j.actamat.2013.01.042.
[8] S. Guo, Q. Hu, C. Ng, C.T. Liu, More than entropy in high-entropy alloys: forming solid solutions or amorphous phase, Intermetallics 41 (2013) 96–103, https://doi.org/10.1016/j.intermet.2013.05.002.
[9] J.W. Yeh, S.K. Chen, S.J. Lin, J.Y. Gan, T.S. Chin, T.T. Shun, C.H. Tsau, S.Y. Chang, Nanostructured high-entropy alloys with multiple principal elements: novel alloy design concepts and outcomes, Adv. Eng. Mater. 6 (2004) 299–303+274, https://doi.org/10.1002/adem.200300567.
[10] K.Y. Tsai, M.H. Tsai, J.W. Yeh, Sluggish diffusion in Co-Cr-Fe-Mn-Ni high-entropy alloys, Acta Mater. 61 (2013) 4887–4897, https://doi.org/10.1016/j.actamat.2013.04.058.
[11] D.A. Porter, K.E. Easterling, Phase Transformations in Metals and Alloys, second ed., Chapman & Hall, London, UK, 1992 https://doi.org/10.1007/978-1-4899-3051-4.
[12] R.W. Hertzberg, R.P. Vinci, J.L. Hertzberg, Deformation and Fracture Mechanics of Engineering Materials, fifth ed., John Wiley & Sons, Inc., Hoboken, New Jersey, 2013 https://doi.org/10.1093/nq/s6-XII.297.185-c.
[13] O. Senkov, G.B. Wilks, D.B. Miracle, C.P. Chuang, P.K. Liaw, Refractory high-entropy alloys, Intermetallics 18 (2010) 1758–1765, https://doi.org/10.1016/j.intermet.2010.05.014.
[14] O.N. Senkov, G.B. Wilks, J.M. Scott, D.B. Miracle, Mechanical properties of Nb 25Mo 25Ta 25W 25 and V 20Nb 20Mo 20Ta 20W 20 refractory high entropy alloys, Intermetallics 19 (2011) 698–706, https://doi.org/10.1016/j.intermet.2011.01.004.
[15] C.C. Juan, M.H. Tsai, C.W. Tsai, C.M. Lin, W.R. Wang, C.C. Yang, S.K. Chen, S.J. Lin, J.W. Yeh, Enhanced mechanical properties of HfMoTaTiZr and HfMoNbTaTiZr refractory high-entropy alloys, Intermetallics 62 (2015) 76–83, https://doi.org/10.1016/j.intermet.2015.03.013.
[16] O.N. Senkov, S. Rao, K.J. Chaput, C. Woodward, Compositional effect on microstructure and properties of NbTiZr-based complex concentrated alloys, Acta Mater. 151 (2018) 201–215, https://doi.org/10.1016/j.actamat.2018.03.065.
[17] J.Y. He, H. Wang, Y. Wu, X.J. Liu, T.G. Nieh, Z.P. Lu, High-temperature plastic flow of a precipitation-hardened FeCoNiCr high entropy alloy, Mater. Sci. Eng. A 686 (2017) 34–40, https://doi.org/10.1016/j.msea.2017.01.027.
[18] W. Li, G. Wang, S. Wu, P.K. Liaw, Creep, fatigue, and fracture behavior of high-entropy alloys, J. Mater. Res. (2018) 1–24, https://doi.org/10.1557/jmr.2018.191.
[19] C. Cao, J. Fu, T. Tong, Y. Hao, P. Gu, H. Hao, L. Peng, Intermediate-temperature creep deformation and microstructural evolution of an equiatomic FCC-structured CoCrFeNiMn high-entropy alloy, Entropy 20 (2018) 960, https://doi.org/10.3390/e20120960.
[20] B. Schuh, F. Mendez-Martin, B. Völker, E.P. George, H. Clemens, R. Pippan, A. Hohenwarter, Mechanical properties, microstructure and thermal stability of a nanocrystalline CoCrFeMnNi high-entropy alloy after severe plastic deformation, Acta Mater. 96 (2015) 258–268, https://doi.org/10.1016/j.actamat.2015.06.025.
[21] W. Zhou, L.M. Fu, P. Liu, X.D. Xu, B. Chen, G.Z. Zhu, X.D. Wang, A.D. Shan, M.W. Chen, Deformation stimulated precipitation of a single-phase CoCrFeMnNi high entropy alloy, Intermetallics 85 (2017) 90–97, https://doi.org/10.1016/j.intermet.2017.02.010.
[22] F. Otto, A. Dlouhý, K.G. Pradeep, M. Kuběnová, D. Raabe, G. Eggeler, E.P. George, Decomposition of the single-phase high-entropy alloy CrMnFeCoNi after prolonged anneals at intermediate temperatures, Acta Mater. 112 (2016) 40–52, https://doi.org/10.1016/j.actamat.2016.04.005.
[23] D. Furrer, H. Fecht, Ni-based superalloys for turbine discs, JOM (J. Occup. Med.) 51 (1999) 14–17, https://doi.org/10.1007/s11837-999-0005-y.
[24] T.M. Pollock, S. Tin, Nickel-based superalloys for advanced turbine engines: chemistry, microstructure and properties, J. Propuls. Power 22 (2006) 361–374, https://doi.org/10.2514/1.18239.
[25] K. Maile, Qualification of Ni-Based alloys for advanced ultra super critical plants, Procedia Eng. 55 (2013) 214–220, https://doi.org/10.1016/j.proeng.2013.03.245.
[26] R.C. Reed, The Superalloys: Fundamentals and Applications, Cambridge University Press, New York, 2006.
[27] V. Shankar, K. Bhanu Sankara Rao, S.L. Mannan, Microstructure and mechanical properties of Inconel 625 superalloy, J. Nucl. Mater. 288 (2001) 222–232, https://doi.org/10.1016/S0022-3115(00)00723-6.
[28] J. Klower, R.U. Husemann, M. Bader, Development of nickel alloys based on alloy 617 for components in 700C power plants, Procedia Eng. 55 (2013) 226–231, https://doi.org/10.1016/j.proeng.2013.03.247.
[29] R.W. Kozar, a. Suzuki, W.W. Milligan, J.J. Schirra, M.F. Savage, T.M. Pollock, Strengthening mechanisms in polycrystalline multimodal nickel-base superalloys, Metall. Mater. Trans. A Phys. Metall. Mater. Sci. 40 (2009) 1588–1603, https://doi.org/10.1007/s11661-009-9858-5.
[30] L. Kovarik, R.R. Unocic, J. Li, P. Sarosi, C. Shen, Y. Wang, M.J. Mills, Microtwinning and other shearing mechanisms at intermediate temperatures in Ni-based superalloys, Prog. Mater. Sci. 54 (2009) 839–873, https://doi.org/10.1016/j.pmatsci.2009.03.010.
[31] T.M. Smith, R.R. Unocic, H. Deutchman, M.J. Mills, Creep deformation mechanism mapping in nickel base disk superalloys, Mater. A. T. High. Temp. 33 (2016) 372–383, https://doi.org/10.1080/09603409.2016.1180858.
[32] B. Cantor, I.T.H. Chang, P. Knight, A.J.B. Vincent, Microstructural development in equiatomic multicomponent alloys, Mater. Sci. Eng. A 375–377 (2004) 213–218, https://doi.org/10.1016/j.msea.2003.10.257.
[33] Z. Zhang, M.M. Mao, J. Wang, B. Gludovatz, Z. Zhang, S.X. Mao, E.P. George, Q. Yu, R.O. Ritchie, Nanoscale origins of the damage tolerance of the high-entropy alloy CrMnFeCoNi, Nat. Commun. 6 (2015) 10143, https://doi.org/10.1038/ncomms10143.
[34] G. Laplanche, A. Kostka, O.M. Horst, G. Eggeler, E.P. George, Microstructure evolution and critical stress for twinning in the CrMnFeCoNi high-entropy alloy, Acta Mater. 118 (2016) 152–163, https://doi.org/10.1016/j.actamat.2016.07.038.
[35] C. Haase, L.A. Barrales-Mora, Influence of deformation and annealing twinning on the microstructure and texture evolution of face-centered cubic high-entropy alloys, Acta Mater. 150 (2018) 88–103, https://doi.org/10.1016/j.actamat.2018.02.048.
[36] Z. Wu, H. Bei, G.M. Pharr, E.P. George, Temperature dependence of the mechanical properties of equiatomic solid solution alloys with face-centered cubic crystal structures, Acta Mater. 81 (2014) 428–441, https://doi.org/10.1016/j.actamat.2014.08.026.
[37] G. Laplanche, A. Kostka, C. Reinhart, J. Hunfeld, G. Eggeler, E.P. George, Reasons for the superior mechanical properties of medium-entropy CrCoNi compared to high-entropy CrMnFeCoNi, Acta Mater. 128 (2017) 292–303, https://doi.org/10.1016/j.actamat.2017.02.036.
[38] J. Miao, C.E. Slone, T.M. Smith, C. Niu, H. Bei, M. Ghazisaeidi, G.M. Pharr, M.J. Mills, The evolution of the deformation substructure in a Ni-Co-Cr equiatomic solid solution alloy, Acta Mater. 132 (2017), https://doi.org/10.1016/j.actamat.2017.04.033.
[39] C. Niu, C.R. LaRosa, J. Miao, M.J. Mills, M. Ghazisaeidi, Magnetically-driven

phase transformation strengthening in high entropy alloys, Nat. Commun. 9 (2018), https://doi.org/10.1038/s41467-018-03846-0.
[40] C.E. Slone, J. Miao, E.P. George, M.J. Mills, Achieving ultra-high strength and ductility in equiatomic CrCoNi with partially recrystallized microstructures, Acta Mater. 165 (2019) 496–507, https://doi.org/10.1016/j.actamat.2018.12.015.
[41] N.D. Evans, P.J. Maziasz, R.W. Swindeman, G.D. Smith, Microstructure and phase stability in INCONEL alloy 740 during creep, Scr. Mater. 51 (2004) 503–507, https://doi.org/10.1016/j.scriptamat.2004.05.047.
[42] S. Zhao, X. Xie, G.D. Smith, S.J. Patel, Research and Improvement on structure stability and corrosion resistance of nickel-base superalloy INCONEL alloy 740, Mater. Des. 27 (2006) 1120–1127, https://doi.org/10.1016/j.matdes.2005.03.015.
[43] OIM Analysis, 2016, Version 8.0.
[44] C.E. Slone, J. Miao, M.J. Mills, Ultra-high strength and ductility from rolling and annealing of a Ni-Cr-Co superalloy, Scr. Mater. 155 (2018) 94–98, https://doi.org/10.1016/j.scriptamat.2018.06.033.
[45] I.M. Lifshitz, V.V. Slyozov, The kinetics of precipitation from supersaturated solid solutions, J. Phys. Chem. Solids 19 (1961) 35–50.
[46] V.C. Wagner, The theory of the aging of precipitation by dissolving (Ostwald ripening), Z. Elektrochem. 65 (1961) 581–591.
[47] K.H. Lo, C.H. Shek, J.K.L. Lai, Recent developments in stainless steels 65 (2009) 39–104, https://doi.org/10.1016/j.mser.2009.03.001.
[48] S.J. Patel, Introduction to Inconel alloy 740: an alloy designed for superheater tubing in coal-fired ultra supercritical boilers, Acta Metall. Sin. (English Lett.) 18 (2005) 479–488.
[50] Y. Ma, F. Yuan, M. Yang, P. Jiang, E. Ma, X. Wu, Dynamic shear deformation of a CrCoNi medium-entropy alloy with heterogeneous grain structures, Acta Mater. 148 (2018) 407–418, https://doi.org/10.1016/j.actamat.2018.02.016.
[51] S. Praveen, J. Wung, P. Asghari-rad, J. Min, H. Seop, Ultra-high tensile strength nanocrystalline CoCrNi equi-atomic medium entropy alloy processed by high-pressure torsion, Mater. Sci. Eng. A 735 (2018) 394–397.
[52] S. Praveen, J.W. Bae, P. Asghari-Rad, J.M. Park, H.S. Kim, Annealing-induced hardening in high-pressure torsion processed CoCrNi medium entropy alloy, Mater. Sci. Eng. A 734 (2018) 338–340, https://doi.org/10.1016/j.msea.2018.07.107.
[53] H.W. Deng, Z.M. Xie, B.L. Zhao, Y.K. Wang, M.M. Wang, J.F. Yang, T. Zhang, Y. Xiong, X.P. Wang, Q.F. Fang, C.S. Liu, Tailoring mechanical properties of a CoCrNi medium-entropy alloy by controlling nanotwin-HCP lamellae and annealing twins, Mater. Sci. Eng. A 744 (2018) 241–246, https://doi.org/10.1016/j.msea.2018.11.143.
[54] B. Schuh, B. Volker, J. Todt, K.S. Kormout, N. Schell, A. Hohenwarter, Influence of annealing on microstructure and mechanical properties of a nanocrystalline CrCoNi medium-entropy alloy, Materials (Basel) 11 (2018), https://doi.org/10.1007/s11661-018-4472-z.
[55] G. Laplanche, S. Berglund, C. Reinhart, A. Kostka, F. Fox, E.P. George, Phase stability and kinetics of σ-phase precipitation in CrMnFeCoNi high-entropy alloys, Acta Mater. 161 (2018) 338–351, https://doi.org/10.1016/j.actamat.2018.09.040.
[56] H. Jiang, J. Dong, M. Zhang, The phase decomposition with related element interaction and redistribution during long term aging of 740H superalloy, J. Alloy. Comp. 782 (2019) 323–333. S0925838818347674.
[57] M.H. Tsai, K.Y. Tsai, C.W. Tsai, C. Lee, C.C. Juan, J.W. Yeh, Criterion for sigma phase formation in Cr- and V-Containing high-entropy alloys, Mater. Res. Lett. 1 (2013) 207–212, https://doi.org/10.1080/21663831.2013.831382.
[58] S. Guo, C. Ng, J. Lu, C.T. Liu, Effect of valence electron concentration on stability of fcc or bcc phase in high entropy alloys, J. Appl. Phys. 109 (2011), https://doi.org/10.1063/1.3587228.
[59] C.K. Sudbrack, L.J. Evans, A. Garg, D.E. Perea, D.K. Schreiber, Characterization of grain boundaries and associated minor phases in disk alloy ME3 exposed at 815 °C, in: Superalloys 2016 Proc. 13th Int. Symp. Superalloys, 2016, pp. 927–936.
[60] C.Y. Barlow, B. Ralph, Observations of cellular transformation products in nickel-base superalloys, J. Mater. Sci. 14 (1979) 2500–2508, https://doi.org/10.1007/BF00737041.
[61] R. Maldonado, E. Nembach, The formation of precipitate free zones and the growth of grain boundary carbides in the nickel-base superalloy NIMONIC PE16, Acta Mater. 45 (1997) 213–224, https://doi.org/10.1016/S1359-6454(96)00139-5.
[62] A. Heckl, S. Cenanovic, M. Göken, R.F. Singer, Discontinuous precipitation and phase stability in Re- and Ru-containing nickel-base superalloys, Metall. Mater. Trans. A Phys. Metall. Mater. Sci. 43 (2012) 10–19, https://doi.org/10.1007/s11661-011-0833-6.
[63] D.H. Bechetti, J.N. DuPont, J.A. Siefert, J.P. Shingledecker, Microstructural evolution and creep-rupture behavior of A-USC alloy fusion welds, Metall. Mater. Trans. A Phys. Metall. Mater. Sci. 47 (2016) 4502–4518, https://doi.org/10.1007/s11661-016-3603-7.
[64] D.H. Bechetti, J.N. DuPont, J.J. de Barbadillo, B.a. Baker, M. Watanabe, Microstructural evolution of INCONEL® alloy 740H® fusion welds during creep, Metall. Mater. Trans. A 46 (2014) 739–755, https://doi.org/10.1007/s11661-014-2682-6.
[65] Q. Xu, T. Cao, F. Ye, F. Xu, H. Li, X. Fang, J. Zhao, Creep-induced microstructural evolution in a nickel-based superalloy designed for advanced ultra-supercritical boilers, Mater. Char. 139 (2018) 311–318, https://doi.org/10.1016/j.matchar.2018.03.008.
[66] H. Li, F. Ye, J. Zhao, T. Cao, F. Xu, Q. Xu, Y. Wang, C. Cheng, X. Min, Grain boundary migration-induced directional coarsening of the γ′ phase in advanced ultra-supercritical superalloy, Mater. Sci. Eng. A 714 (2018) 172–178, https://doi.org/10.1016/j.msea.2017.12.089.
[67] J. Wadsworth, O.a. Ruano, O.D. Sherby, Denuded zones, diffusional creep, and grain boundary sliding, Metall. Mater. Trans. A 33 (2002) 219–229, https://doi.org/10.1007/s11661-002-0084-7.
[68] D.B. Williams, E.P. Butler, Grain boundary discontinuous precipitation reactions, Int. Mater. Rev. 26 (1981) 153–183, https://doi.org/10.1179/095066081790149267.
[69] R.A. Fournelle, Discontinuous coarsening of lamellar cellular precipitate in an austenitic Fe-30 wt .% Ni-6 wt .% Ti alloy - I. morphology, Acta Metall. 27 (1979) 1135–1145.
[70] B.C. De Cooman, Y. Estrin, S. Kyu, Twinning-induced plasticity (TWIP) steels, Acta Mater. 142 (2018) 283–362, https://doi.org/10.1016/j.actamat.2017.06.046.
[71] S.F. Liu, Y. Wu, H.T. Wang, J.Y. He, J.B. Liu, C.X. Chen, X.J. Liu, H. Wang, Z.P. Lu, Stacking fault energy of face-centered-cubic high entropy alloys, Intermetallics 93 (2018) 269–273, https://doi.org/10.1016/j.intermet.2017.10.004.
[72] N. Saunders, Z. Guo, X. Li, A.P. Miodownik, J.P. Schille, Using JMatPro to model materials properties and behavior, JOM (J. Occup. Med.) (2003) 60–65.
[73] L. Delehouzee, A. Deruyttere, The stacking fault density in solid solutions based on copper, silver, nickel, aluminium, and lead, Acta Metall. 15 (1967) 727–734.
[74] P.C. Gallagher, The influence of alloying, temperature, and related effects on the stacking fault energy, Metall. Trans. I (1970) 2429–2461.